Stability of generalized Kolmogorov flow in a channel

Francesco Romanò[a)]

AFFILIATIONS

Univ. Lille, CNRS, ONERA, Arts et Métiers Institute of Technology, Centrale Lille, UMR 9014 - LMFL - Laboratoire de Mécanique des Fluides de Lille - Kampé de Fériet, 59000, Lille, France

[a)]Author to whom correspondence should be addressed: francesco.romano@ensam.eu

ABSTRACT

The Kolmogorov flow is a paradigmatic model flow used to investigate the transition from laminar to turbulent regimes in confined and, especially, in unbounded domains. It represents a solution of the forced Navier–Stokes equation, where the forcing term is sinusoidal. The resulting velocity profile is also sinusoidal with the same wavenumber of the forcing term. In this study, we generalize the Kolmogorov flow making use of a generic forcing term defined by a Fourier series that bridges the classical Kolmogorov flow to an arbitrary even-degree power-law profile. Thereafter, we perform a linear stability analysis on the power-law profiles for exponents, $\alpha = 2$, 4, 6, 8, and 10, and the corresponding generalized Kolmogorov flows, varying the truncation index K of the Fourier series. Several neutral stability curves are computed numerically for wall-bounded flows and the relevant critical conditions are compared in terms of critical Reynolds number, critical wavelength, and eigenspectrum at criticality. The most dangerous perturbations are thoroughly characterized, and we identify three qualitatively different most dangerous modes, depending on α, K, the Reynolds number, and the perturbation wavelength.

I. INTRODUCTION

Parallel shear flows are solutions of the Navier–Stokes equation with a velocity field $\boldsymbol{u}$ in the form $\boldsymbol{u} = u(y,z)\boldsymbol{e}_x$, where x denotes the streamwise direction and y and z are the coordinates orthogonal to x. These flows can be realized by means of either a pressure gradient, moving boundaries or a body force directed along x. Classical examples of parallel shear flows are the boundary-driven Couette flow, the pressure-driven plane Poiseuille and Hagen–Poiseuille flows, and the body-force-driven Kolmogorov flow. These simple solutions of the Navier–Stokes equation represent paradigmatic flows widely used for investigating hydrodynamic instabilities[1] and transition of laminar shear flows to turbulence either in confined[2] or in periodic domains.[3]

The Kolmogorov flow is a flow driven by a periodic (sinusoidal) monochromatic force and it was first introduced by Kolmogorov[4] for studying hydrodynamic instabilities and transition to turbulence in spatially periodic domains. Experimental realizations of the Kolmogorov flow are done using magnetohydrodynamic forcing with sinusoidal magnetic fields.[5–7] More recently, adding a Coriolis forcing term, the Kolmogorov flow has been employed as a barotropic ocean model,[8–10] and experimental realizations of the Kolmogorov flow are also made by means of soap films.[11]

Meshalkin and Sinai[12] carried out the first analytical stability analysis of the two-dimensional Kolmogorov flow for a unitary wavenumber of the forcing term. For a domain with streamwise-to-wavelength aspect ratio equal to $L_x/Ly = 1/\Gamma$, they found that the Kolmogorov flow is stable for $\Gamma \geq 1$ and it becomes unstable for $\Gamma < 1$ with $\mathrm{Re} = \mathrm{Re}_c \to \sqrt{2}$ for $\Gamma \to 0$, where Re is the Reynolds number. These results found confirmation in the studies of Iudovich[13] and Marchioro,[14] who further extended them by demonstrating that the Kolmogorov flow is globally stable for $\Gamma \geq 1$. Other studies on the stability of the Kolmogorov flow carried out a bifurcation analysis and showed that the primary bifurcation of the Kolmogorov flow is a supercritical pitchfork bifurcation.[15] These studies were further extended to higher Re,[16] and the exact expressions were determined for the second derivatives of the bifurcation components at the bifurcation points.[17] Fundamental computational contributions are due to Nagatou,[18] who focused on the stability of the bifurcating solutions proposing an algorithm to bracket the critical Reynolds number for given Γ with an accuracy almost up to machine precision. Further generalizations of the classical periodic monochromatic Kolmogorov flow consist of dealing with rhombic cells, either in viscous or inviscid regimes,[19,20] flow confinements,[21,22] time-periodic forcing[23] non-Newtonian stress tensors,[24] and three-dimensional flows.[25–27]

Since its introduction, the Kolmogorov flow has been employed for studying the transition to Newtonian and non-Newtonian turbulence of shear flows. High-Reynolds-number regimes have been targeted by several studies that identified how the Kolmogorov flow becomes chaotic and then turbulent upon an increase of Re, undergoing a sequence of bifurcations and a number of flow patterns.[3,28–30] Moreover, owing to its versatility, the Kolmogorov flow has been assumed as a model flow for investigating the effect on the transition to turbulence of the forcing wavelength,[3,29] the flow confinement,[21,31] the thermal stratification,[32] the flow compressibility,[31,33] as well as of non-Newtonian stress tensors including viscoelastic[34] or granular[35] constitutive models.

In this paper, we propose a generalization of the Kolmogorov flow, in which the forcing term is given by a summation of K Fourier modes. In a closed channel confined by parallel rigid walls, the stability diagram of the generalized Kolmogorov flow will turn the neutral stability curve of the classical Kolmogorov flow (for $K = 1$) into the stability curve of the Poiseuille flow (for $K \to \infty$). Thereafter, this same approach is used to further extend the generalized Kolmogorov flow to arbitrary even-degree power-law flows with the aim of providing a generalized model framework for the investigation of body-force-driven flows. The paper is organized as follows: Sec. II formulates the mathematical problem, generalizes the Kolmogorov flow, and briefly recalls the Orr–Sommerfeld equation used to carry out the linear stability analysis, and Sec. III describes and validates the numerical code used to solve the eigenvalue problem at the core of the linear stability analysis. The results of our numerical study are presented and discussed in Sec. IV. Finally, the conclusions of our study are drawn in Sec. V.

II. PROBLEM FORMULATION

The incompressible flow of a fluid with constant density ρ and kinematic viscosity ν is considered. Scaling lengths, time, velocity, pressure, and body forces by H, H/U, U, ρU^2, and $\rho U^2/H$, the non-dimensional continuity and Navier–Stokes equations read

$$\nabla \cdot \boldsymbol{u} = 0, \tag{1a}$$

$$\frac{\partial \boldsymbol{u}}{\partial t} + \boldsymbol{u} \cdot \nabla \boldsymbol{u} = -\nabla p + \frac{1}{\mathrm{Re}} \nabla^2 \boldsymbol{u} + \boldsymbol{f}, \tag{1b}$$

where $\boldsymbol{x} = (x, y, z)$ and t are the space and time coordinates, $\boldsymbol{u} = (u, v, w)$ and p denote the velocity and pressure fields, $\boldsymbol{f} = (f_x, f_y, f_z)$ is a body force, and $\mathrm{Re} = UH/\nu$ is the Reynolds number.

A. Generalized Kolmogorov flow

When the forcing term is monochromatic and sinusoidal, i.e., $\boldsymbol{f} = (\mathrm{Re}^{-1}\pi^2 \sin[\pi(y+1)/2]/4,\ 0,\ 0)$, the (1) admits a steady plane-flow solution which is itself unidirectional and sinusoidal in velocity, i.e., $\boldsymbol{u} = (\sin[\pi(y+1)/2],\ 0,\ 0)$, where U and H are assumed as the maximum flow velocity and a quarter of the forcing wavelength, respectively. This flow is known as Kolmogorov flow and it is commonly extended to periodic domains to investigate the transition to turbulence without including any solid boundary. In a plane channel flow, the Kolmogorov flow can be used as first-mode-approximation model of the Poiseuille flow [see Fig. 1(a)]. In this sense, for unbounded domains, the Kolmogorov flow approximates the flow

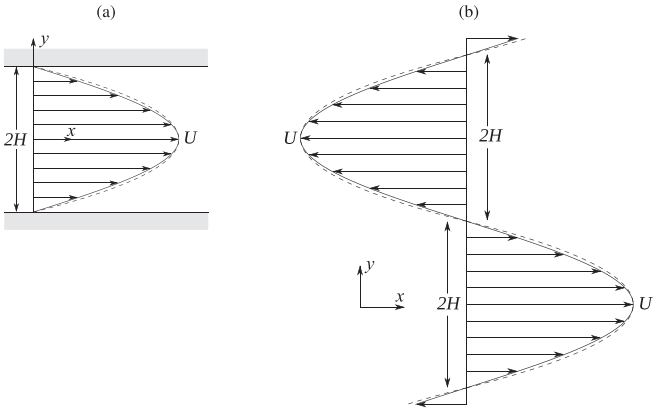

FIG. 1. (a) Kolmogorov (solid line) and Poiseuille (dashed line) flow in a plane channel flow. The channel walls are delimited by solid lines and gray rectangles. (b) Periodic Kolmogorov flow (solid line) and antisymmetric Poiseuille flows matched in slope (dashed line). The domain is unbounded. In both the sub-figures, the arrows denote the velocity vector field.

consisting of antisymmetric Poiseuille flows matched in slope [see Fig. 1(b)],

$$\begin{aligned} f_x &= \frac{\pi^2 \sin[\pi(y+1)/2]}{4\mathrm{Re}}, \\ u &= \sin[\pi(y+1)/2] \\ &\approx \begin{cases} 1-(y-4n)^2 & \text{if } y \in [-1,\ 1] + 4n \\ -1+(y-4n+2)^2 & \text{if } y \in [-3, -1] + 4n, \end{cases} \end{aligned} \tag{2}$$

where $n \in \mathbb{Z}$. Within our scaling, U also represents the maximum velocity magnitude of the anti-symmetric Poiseuille flows and H is half of the height of each Poiseuille flow sub-domain [see Fig. 1(b)].

Two generalizations of the Kolmogorov flow are discussed as follows: (i) the consideration of higher harmonics of the Fourier expansion to bridge the classical Kolmogorov to the Poiseuille flow and (ii) the investigation of even-degree polynomial flows of degree higher than two. The former point is of interest since remarkable differences are observed in the linear stability of Kolmogorov and Poiseuille flows for confined geometries, and we aim at characterizing how such differences decay by employing more than one Fourier mode. This same generalization could then be used in further studies to investigate the two-dimensional transition to turbulence for higher-order approximation of the anti-symmetric Poiseuille flows in unbounded domains. The corresponding Fourier series reads

$$\begin{aligned} u &= \frac{32}{\pi^3} \sum_{k=1}^{\infty} \frac{1}{(2k-1)^3} \sin[\pi(2k-1)(y+1)/2] \\ &= \begin{cases} 1-(y-4n)^2 & \text{if } y \in [-1,\ 1] + 4n \\ -1+(y-4n+2)^2 & \text{if } y \in [-3, -1] + 4n. \end{cases} \end{aligned} \tag{3}$$

The second generalization considers anti-symmetric even-degree polynomial flows of arbitrary order matched in slope as done for the Poiseuille flow [see Fig. 2(b)]. The corresponding Fourier series represents a generalized form of (3),

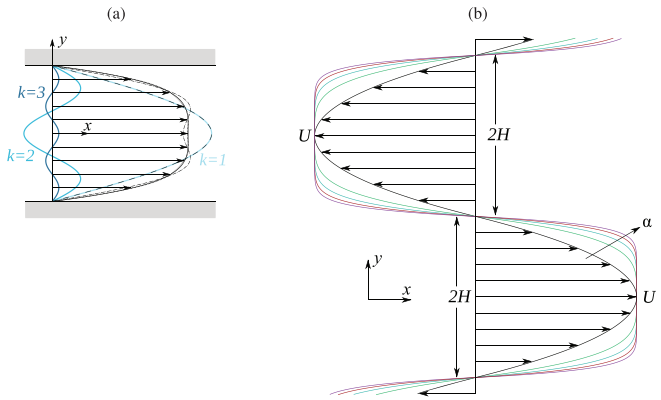

FIG. 2. (a) Power-law flow for $\alpha = 4$ (solid black line), first three Fourier modes (blue lines, i.e., $k = 1$, $k = 2$ and $k = 3$ of (4)), truncation of the Fourier series to the first (dashed black line), second (dashed–dotted black line), and third (dotted black line) Fourier mode. The channel walls are delimited by solid line and gray rectangles. (b) Periodic antisymmetric power-law flows matched in slope for $\alpha = 2$ (black, Poiseuille flow), $\alpha = 4$ (green), $\alpha = 6$ (light blue), $\alpha = 8$ (red), and $\alpha = 10$ (violet). The domain is unbounded. In both the sub-figures, the arrows denote the velocity vector field.

$$u = \sum_{k=1}^{\infty}\sum_{m=1}^{\alpha/2} \frac{(-1)^{m+1} 2^{2(m+1)} \prod_{l=0}^{2m-1}(\alpha - l)}{[(2k-1)\pi]^{2m+1}} \sin[\pi(2k-1)(y+1)/2]$$
$$= \begin{cases} 1-(y-4n)^{\alpha} & \text{if } y \in [-1,\ 1] + 4n \\ -1+(y-4n+2)^{\alpha} & \text{if } y \in [-3,-1] + 4n, \end{cases} \tag{4}$$

where $\alpha = 2\gamma$ and $\gamma \in \mathbb{N}$. Figure 2(a) depicts the first three modes of (4) for $\alpha = 4$ for a confined channel flow. The forcing term corresponding to (4) reads

$$f_x = -\frac{1}{\mathrm{Re}}\frac{\partial^2 u}{\partial y^2}$$
$$= \frac{1}{\mathrm{Re}}\sum_{k=1}^{\infty}\sum_{m=1}^{\alpha/2} \frac{(-1)^{m+1} 2^{2(m-1)} \prod_{l=0}^{2m-1}(\alpha - l)}{[(2k-1)\pi]^{2m-1}} \sin[\pi(2k-1)(y+1)/2]. \tag{5}$$

The rationale at the basis of the second generalization consists of proposing a model flow for studying the relaminarization observed for flat profile flows[36] or for investigating the transition to turbulence of forced flows.

B. Linear stability analysis

The plane shear flow defined in (4) is assumed as steady basic flow, $\boldsymbol{u}_0 = (u_0(y),\ 0,\ 0)$. Considering an infinitesimal perturbation $(\tilde{\boldsymbol{u}},\ \tilde{p})$, the linear stability equations of the two-dimensional basic flow read

$$\nabla \cdot \tilde{\boldsymbol{u}} = 0, \tag{6a}$$

$$\frac{\partial \tilde{\boldsymbol{u}}}{\partial t} + \boldsymbol{u}_0 \cdot \nabla \tilde{\boldsymbol{u}} + \tilde{\boldsymbol{u}} \cdot \nabla \boldsymbol{u}_0 = -\nabla \tilde{p} + \frac{1}{\mathrm{Re}} \nabla^2 \tilde{\boldsymbol{u}}. \tag{6b}$$

Since the coefficients of (6) do not depend on time and z, the solution $(\tilde{\boldsymbol{u}},\ \tilde{p})$ admits an exponential ansatz in t and z. Moreover, for plane-parallel basic flows, the infinitesimal perturbation has the form of oblique waves,

$$\tilde{\boldsymbol{q}} = (\tilde{\boldsymbol{u}},\ \tilde{p}) = (\hat{\boldsymbol{u}},\ \hat{p}) e^{i(\sigma x + \beta z) - i\omega t} + c.c. = \hat{\boldsymbol{q}} e^{i(\sigma x + \beta z) - i\omega t} + c.c., \tag{7}$$

where σ and $\beta \in \mathbb{R}$, $\omega \in \mathbb{C}$, $\hat{\boldsymbol{q}} = (\hat{\boldsymbol{u}}, \hat{p})$ depends only on y, and $c.c.$ denotes the complex conjugate ansatz. Plugging (7) in (6), the resulting three-dimensional linear stability equations can be further simplified to an equivalent two-dimensional problem by the following substitution of variables:

$$\bar{\sigma} = \sqrt{\sigma^2 + \beta^2}, \quad \bar{\omega} = \omega\,\sigma / \sqrt{\sigma^2 + \beta^2}, \quad \overline{\mathrm{Re}} = \mathrm{Re}\,\sigma / \sqrt{\sigma^2 + \beta^2}. \tag{8}$$

Without loss of generality, we therefore will remove β from the perturbation ansatz, solve the stability problem in terms of $\bar{\sigma}$, $\bar{\omega}$, and $\overline{\mathrm{Re}}$, and simplify the notation by removing the overline sign in (8). The equivalent two-dimensional problem can be reformulated in terms of the Orr–Sommerfeld equation, which characterizes the infinitesimal streamfunction perturbation, $\tilde{\psi} = \hat{\psi} e^{i\sigma x - i\omega t} + c.c.$, where $\partial_y \hat{\psi} = \hat{u}$ and $-i\sigma\hat{\psi} = \hat{v}$, by the following single-equation eigenvalue problem:

$$(u_0 - c)\left(\frac{\partial}{\partial y^2} - \sigma^2\right)\hat{\psi} + \hat{\psi}\frac{\partial u_0}{\partial y^2} = \frac{1}{i\sigma\mathrm{Re}}\left(\frac{\partial}{\partial y^2} - \sigma^2\right)^2 \hat{\psi}, \tag{9}$$

where $c = \omega/\sigma \in \mathbb{C}$ is the wave speed. Since we target the stability analysis for confined flows, at the walls we set no-slip boundary conditions, i.e., $\hat{\psi} = \partial_y \hat{\psi} = 0$ at $y = -1$ and $y = 1$. We stress that, since the Orr-Sommerfeld equation does not include neither the pressure nor the forcing term, it is irrelevant for the flow stability how the basic flow profile u_0 has been generated.[37]

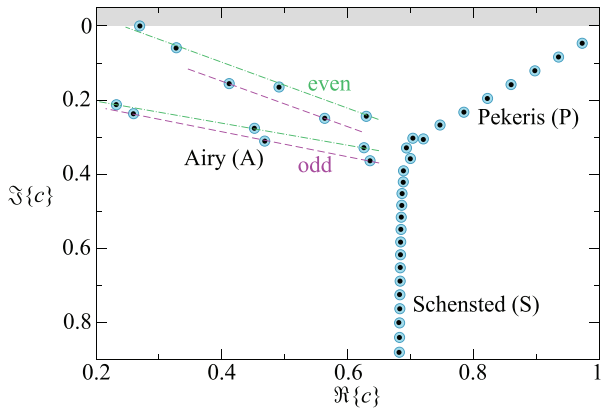

FIG. 3. Eigenspectrum computed by our code (black) and by Ref. 38 (light blue) for the critical conditions of the Poiseuille flow, i.e., $(\mathrm{Re}_c, \sigma_c) = (5772,\ 1.026)$. The three branches of the eigenspectrum are denoted Airy (A), the Schensted (S), and the Pekeris (P) branches. The Airy branch distinguishes two kinds of eigenmodes: symmetric (even, green) and antisymmetric (odd, magenta).

III. NUMERICAL METHOD

The collocation spectral method employed to discretize the linear system (9) relies on Chebyshev–Gauss–Lobatto nodes. The number of spectral nodes is denoted by N. After assembling the matrices that

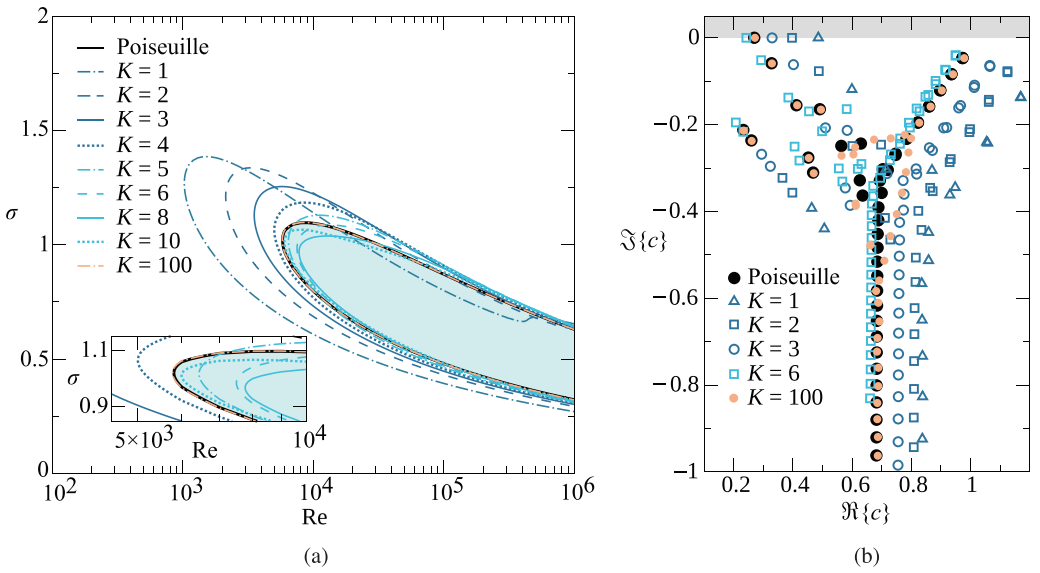

FIG. 4. (a) Neutral stability curves for Poiseuille flow (thick black solid line with unstable region filled in light blue) and generalized Kolmogorov flow (4) for $\alpha = 2$ and truncation index: $K = 1$ (dark-blue dashed–dotted line), $K = 2$ (dark-blue dashed line), $K = 3$ (dark-blue solid line), $K = 4$ (dark-blue dotted line), $K = 5$ (light-blue dashed–dotted line), $K = 6$ (light-blue dashed line), $K = 8$ (light-blue solid line), $K = 10$ (light-blue dotted line), and $K = 100$ (peach dashed–dotted line). (b) Eigenspectrum of the critical conditions for Poiseuille flow (black bullets) and generalized Kolmogorov flow (4) for $\alpha = 2$ and truncation index: $K = 1$ (dark-blue triangles), $K = 2$ (dark-blue squares), $K = 3$ (dark-blue circles), $K = 6$ (light-blue circles), and $K = 100$ (peach bullets). The gray area denotes the unstable domain, i.e., $\Im\{c\} > 0$.

define the discrete form of the generalized eigenvalue problem, the eigenvalues and eigenvectors are computed using the function eig of Matlab.

Figure 3 demonstrates that using $N = 200$ Chebyshev–Gauss–Lobatto nodes provides an excellent agreement of the discrete eigenspectrum at criticality for the Poiseuille flow between our code (black) and the reference data[38] (light blue). The eigenvalues of the two solvers are in excellent agreement for all three branches of the eigenspectrum, i.e., the Airy (A), the Schensted (S), and the Pekeris (P) branches. After a mesh convergence test (not shown), we decided to employ $N = 100$ for all the results presented in Sec. IV, increasing the number of Chebyshev–Gauss–Lobatto nodes to $N = 200$ whenever critical conditions are computed or most dangerous modes are depicted.

IV. RESULTS AND DISCUSSION

The generalized form of the Kolmogorov flow reported in (4) is here assumed as basic state $\boldsymbol{u}_0$. Making use of the spectral solver presented in Sec. III, we determine the stability limits of the generalized Kolmogorov flow for several truncates of the Fourier series (4). In the following, the order of truncation is denoted by the truncation index K, the two-dimensional parameter space $(\sigma, \mathrm{Re}) \in [0, 2] \times [5 \times 10^2, 10^6]$ is explored with steps in σ of 1%, i.e., $\Delta\sigma = 0.01$, and steps in Reynolds of 500, i.e., $\Delta\mathrm{Re} = 500$. The resolution in Re is thereafter increased whenever the critical conditions are determined.

A. Stability of generalized Kolmogorov flow for Poiseuille flow

The stability of generalized Kolmogorov flow is investigated, setting $\alpha = 2$ in (4), i.e., for a Fourier series that tends to the Poiseuille flow. Figure 4(a) shows the neutral stability boundaries for a Poiseuille flow (a thick solid black line) confined within a rigid channel of dimensional height $2H$. The light-blue area denotes the unstable region of the Poiseuille flow and the turning point characterizes the critical conditions $(\mathrm{Re}_c, \sigma_c) = (5772, 1.026)$. These conditions are poorly approximated by (4) when truncating the Fourier series to the first term (Kolmogorov flow), such that σ_c is overestimated of about 30% and Re_c is underestimated of almost a factor 6. The unstable region of the confined Kolmogorov flow is found to grow in comparison to the unstable region of the Poiseuille flow. The two curves intersect each other at $(\mathrm{Re}, \sigma) \approx (2 \times 10^4, 1)$, and the neutral stability boundary for $K = 1$ underestimates the upper limit of the unstable region for Poiseuille flow for $\mathrm{Re} \gtrsim 2 \times 10^4$. Upon an increase in the

TABLE I. Critical Reynolds (Re_c) and critical wavelength (σ_c) for the generalized Kolmogorov flow (4) for $\alpha = 2$ and truncation index K.

Modes	Re_c	σ_c
$K = 1$	1025	1.27
$K = 2$	2128	1.21
$K = 3$	3523	1.13
$K = 4$	5016	1.06
$K = 5$	6438	1.02
$K = 6$	7500	0.99
$K = 8$	7767	0.97
$K = 10$	5993	1.01
$K = 100$	5767	1.03
Poiseuille	5772	1.026

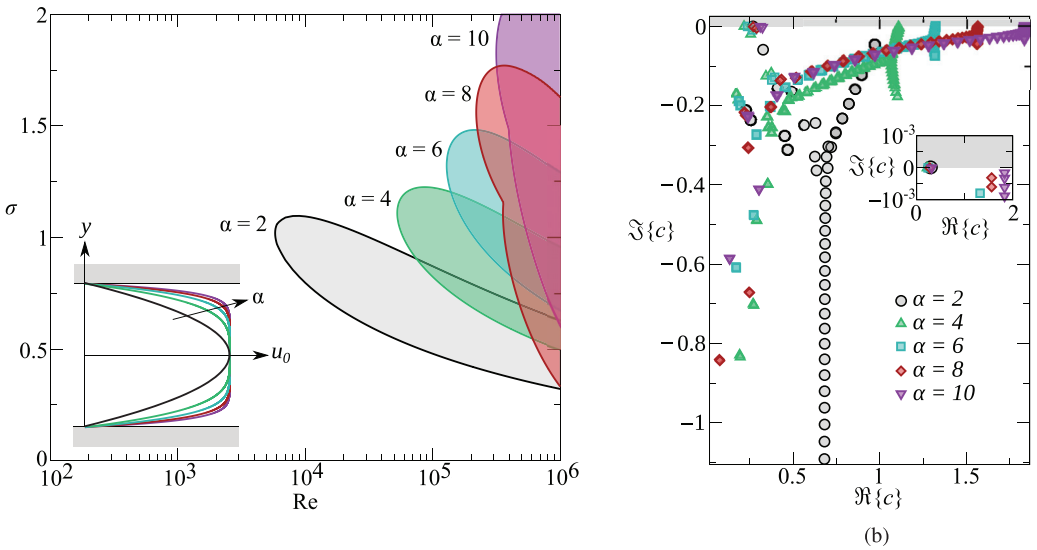

FIG. 5. (a) Neutral stability curves for even-degree power-law flows: $\alpha = 2$ (Poiseuille flow, thick black solid line with unstable region filled in light gray), $\alpha = 4$ (thick green solid line with unstable region filled in light green), $\alpha = 6$ (thick light-blue solid line with unstable region filled in light blue), $\alpha = 8$ (thick red solid line with unstable region filled in light red), and $\alpha = 10$ (thick violet solid line with unstable region filled in light violet). The inset at the bottom-left corner depicts the basic states upon a change of α. The velocity profiles are color coded like the stability curves. (b) Eigenspectrum of the critical conditions for $\alpha = 2$ (Poiseuille flow, gray bullet), $\alpha = 4$ (light green triangles), $\alpha = 6$ (light blue squares), $\alpha = 8$ (light red diamonds), and $\alpha = 10$ (light violet triangles). The gray area denotes the unstable domain, i.e., $\Im\{c\} > 0$.

TABLE II. Critical Reynolds (Re_c) and critical wavelength (σ_c) for the even-degree power-law flows $u_0 = 1 - y^\alpha$ for $\alpha = 2$, 4, 6, 8, and 10. A further accuracy check on the $(\alpha = 10)$-profile shows that the relative difference between Re_c computed using $N = 300$ and $N = 200$ is smaller than 0.3%.

Power flow	Re_c	σ_c
$\alpha = 2$	5772	1.026
$\alpha = 4$	52 745	1.11
$\alpha = 6$	128 831	1.32
$\alpha = 8$	219 483	1.56
$\alpha = 10$	315 494	1.83

truncation index K of the generalized Kolmogorov flow, the area of the unstable region reduces up to becoming smaller than the unstable area for Poiseuille flow [see, e.g., $K = 8$ in Fig. 4(a)]. Increasing further the truncation index of (4), the unstable region inverts its area-decreasing trend and approaches the neutral stability curve of the Poiseuille flow already well approximated by $K = 10$. For $K = 100$, we do not observe any remarkable difference between the unstable region of (4) and the corresponding one of the Poiseuille flow [cf. peach and black lines in Fig. 4(a)]. However, focusing on the critical conditions demonstrates that the generalized Kolmogorov flow for $K = 100$ slightly underestimates the critical Reynolds number and overestimates the wavelength of the Poiseuille flow (see Table I).

The real and imaginary parts of the most unstable eigenvalue corresponding to the critical conditions reported in Table I are depicted in Fig. 4(b). Despite the deviation in terms of Re_c and σ_c for different truncation indices K, all the eigenspectra are qualitatively similar. They all admit the Y-shape spectrum characteristic of the Poiseuille flow, and they all become unstable on the left branch of the spectrum due to an even Airy mode. This is demonstrated in Fig. 4(b) by the markers lying in the gray region ($\Im\{c\} \geq 0$). Upon an increase in the truncation index K, the most significant quantitative difference between the eigenspectra is represented by a shift of the real part of the eigenspectrum. For low truncation indices, the critical wavelength of the generalized Kolmogorov flow is larger than the one for Poiseuille flow (see Table I) and, correspondingly, the eigenspectrum shifts toward larger real parts, leading to critical conditions with a higher oscillatory frequency. On the other hand, for $K > 5$, the critical wavelength of the generalized Kolmogorov flow is smaller than the corresponding σ_c of the Poiseuille flow and the oscillatory frequencies of the critical modes of the generalized Kolmogorov flow become smaller than the critical frequency of the Poiseuille flow.

B. Stability of even-degree power-law flows

The even-degree power-law profiles considered as generalization of the pressure-driven Poiseuille flow do not represent exact solutions of the Navier–Stokes equation without a forcing term. However, they become solutions of the forced Navier–Stokes equation if the forcing term equals $\boldsymbol{f} = (f_x, f_y, f_z) = (-\mathrm{Re}^{-1}\partial_y^2 u_0, 0, 0)$. Moreover, they represent the limit for $K \to \infty$ of (4) and therefore we characterize their stability diagram in Fig. 5(a). Upon an increase in the exponent α, we find a remarkable stabilization of the shear flow whose critical Reynolds number increases of about two orders of magnitude passing from $\mathrm{Re}_c \approx 5 \times 10^3$ for $\alpha = 2$ to $\mathrm{Re}_c \approx 3 \times 10^6$ for $\alpha = 10$. A precise quantification of the critical conditions for $\alpha = 2$, 4, 6, 8, and 10 is reported in Table II. Along with such an increase in the basic flow stability, the range of σ for which the flow is unstable broadens and the critical wavelength shifts toward higher σ_c. This stabilization effect is due to the shrinkage of the energy transfer region between the basic

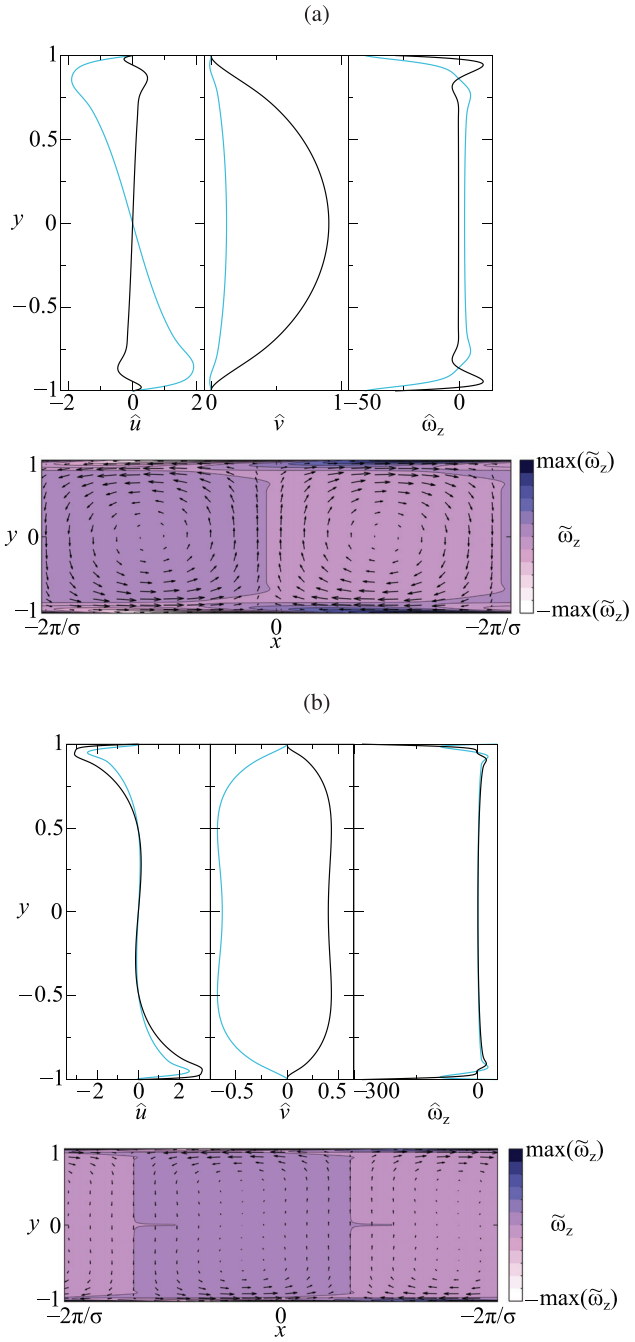

FIG. 6. Top panels: real (black) and imaginary (light blue) parts of the neutral eigenmode in terms of $\hat{u}$ (left), $\hat{v}$ (center), and $\hat{\omega}_z$ (right). Bottom panel: the most dangerous perturbation depicted in terms of vorticity and velocity field (arrows). Critical conditions for the power-law basic state $u_0 = 1 - y^\alpha$ for $\alpha = 2$ (a) and $\alpha = 4$ (b).

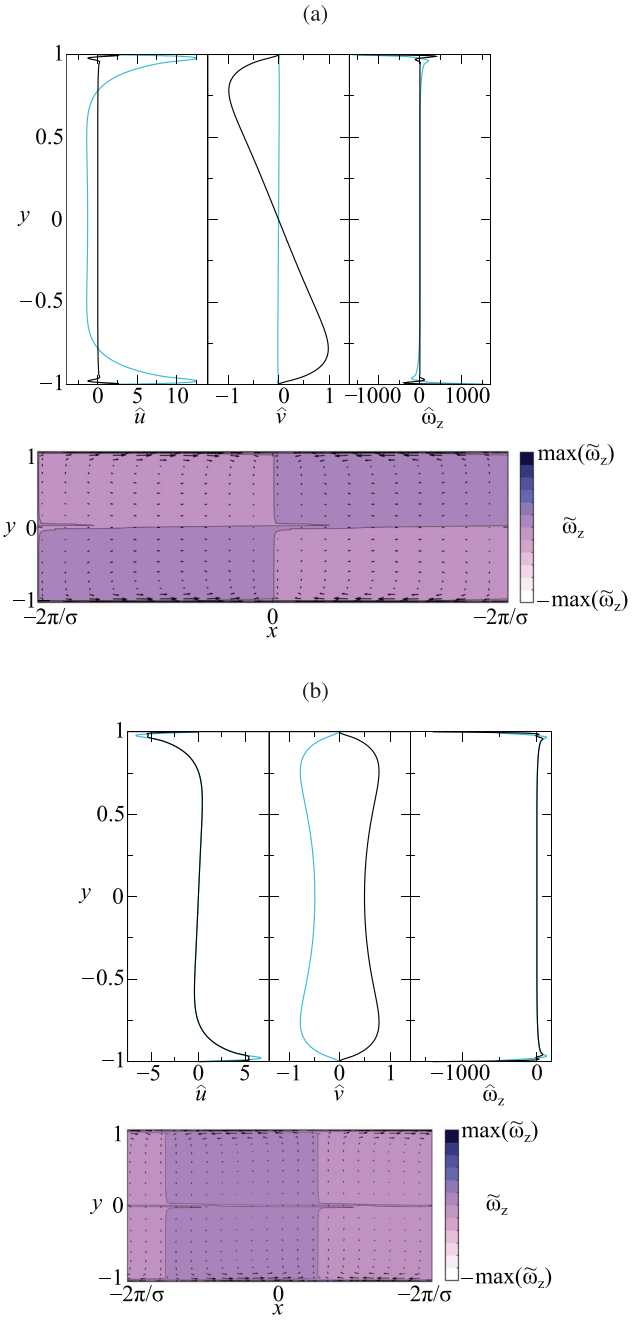

FIG. 7. Top panels: real (black) and imaginary (light blue) parts of the neutral eigenmode in terms of $\hat{u}$ (left), $\hat{v}$ (center), and $\hat{\omega}_z$ (right). Bottom panel: the most dangerous perturbation depicted in terms of vorticity and velocity field (arrows). Neutral conditions $(\mathrm{Re}, \sigma) = (366\,400,\ 1.00)$ for the power-law profile for $\alpha = 8$ (a) and critical conditions for $\alpha = 8$ (b).

state and the flow perturbation. In fact, the y-range for which $d_y u_0 \approx 0$ increases upon an increase of α leading to the most dangerous perturbations whose wall-normal derivatives $\partial_x(\tilde{u}, \tilde{v})$ and $\partial_y(\tilde{u}, \tilde{v})$ become significant only near the channel walls. This is demonstrated in Fig. 6 that depicts the critical modes for $\alpha = 2$ [Fig. 6(a)] and $\alpha = 4$ [Fig. 6(b)]. The top panels show the real (black) and the imaginary (light blue) parts of the eigenmode in terms of x-velocity, $\hat{u}$, y-velocity, $\hat{v}$, and vorticity, $\hat{\omega}_z = i\sigma\hat{v} - \partial_y\hat{u}$, whereas the bottom panel depicts

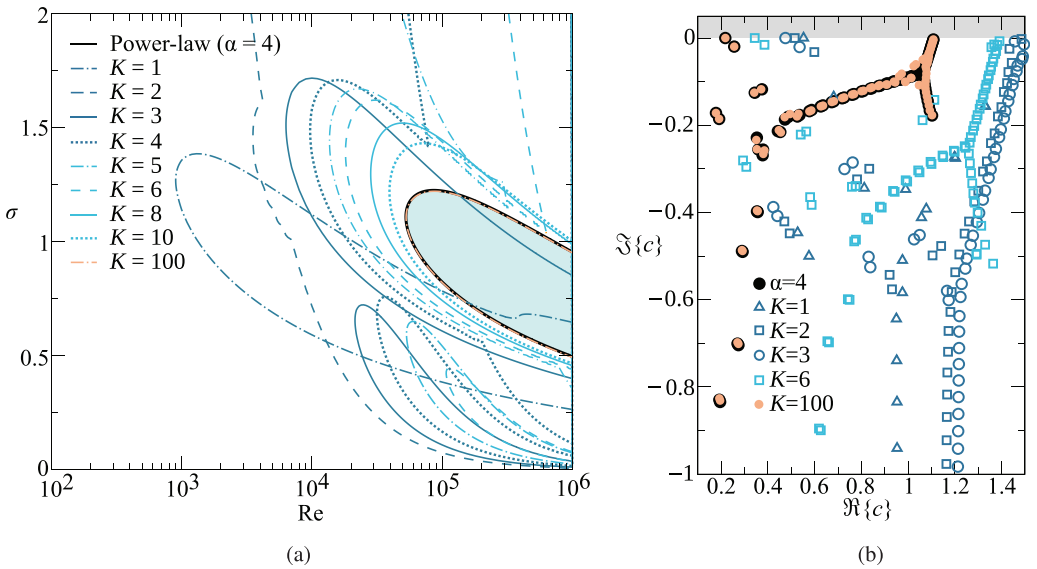

FIG. 8. Neutral stability curves for the power-flow for $\alpha = 4$ (thick black solid line with unstable region filled in light blue) and generalized Kolmogorov flow (4) for $\alpha = 4$ and truncation index: $K = 1$ (dark-blue dashed–dotted line), $K = 2$ (dark-blue dashed line), $K = 3$ (dark-blue solid line), $K = 4$ (dark-blue dotted line), $K = 5$ (light-blue dashed–dotted line), $K = 6$ (light-blue dashed line), $K = 8$ (light-blue solid line), $K = 10$ (light-blue dotted line), and $K = 100$ (peach dashed–dotted line). (b) Eigenspectrum of the critical conditions for the power-flow for $\alpha = 4$ (black bullets) and generalized Kolmogorov flow (4) for $\alpha = 4$ and truncation index: $K = 1$ (dark-blue triangles), $K = 2$ (dark-blue squares), $K = 3$ (dark-blue circles), $K = 6$ (light-blue circles), and $K = 100$ (peach bullets). The gray area denotes the unstable domain, i.e., $\Im c > 0$.

TABLE III. Critical Reynolds (Re_c) and critical wavelength (σ_c) for the generalized Kolmogorov flow (3) of the power-4 profile ($\alpha = 4$) with truncation index K.

Modes	Re_c	σ_c
$K = 1$	901	1.27
$K = 2$	3507	1.46
$K = 3$	6292	1.51
$K = 4$	9679	1.49
$K = 5$	13 649	1.44
$K = 6$	18 133	1.39
$K = 8$	28 308	1.30
$K = 10$	39 458	1.22
$K = 100$	52 941	1.11
$\alpha = 4$	52 745	1.11

one period of the most dangerous perturbation employing 12 contours of vorticity, $\tilde{\omega}_z$, and the velocity vector field ($\tilde{\boldsymbol{u}}$, arrows).

The eigenspectra at criticality are compared in Fig. 5(b). The Y-shape spectrum characteristic of the Poiseuille flow turns into an H-shape spectrum with a long branch at low oscillation frequencies and a short one at high oscillation frequencies. Regardless of the even-degree power-flow exponent α, all the spectra become unstable at low frequencies, as depicted in the inset of Fig. 5(b). The remarkable feature observed for $\alpha = 8$ and 10 is that the neutral stability curve is not as smooth as for $\alpha = 2$, 4, and 6. This results from the intersection of two neutral stability branches due to the presence of two different unstable eigenmodes both emerging from the left branch of the H-shaped eigenspectrum. Figure 7 depicts the neutral modes for $\alpha = 8$

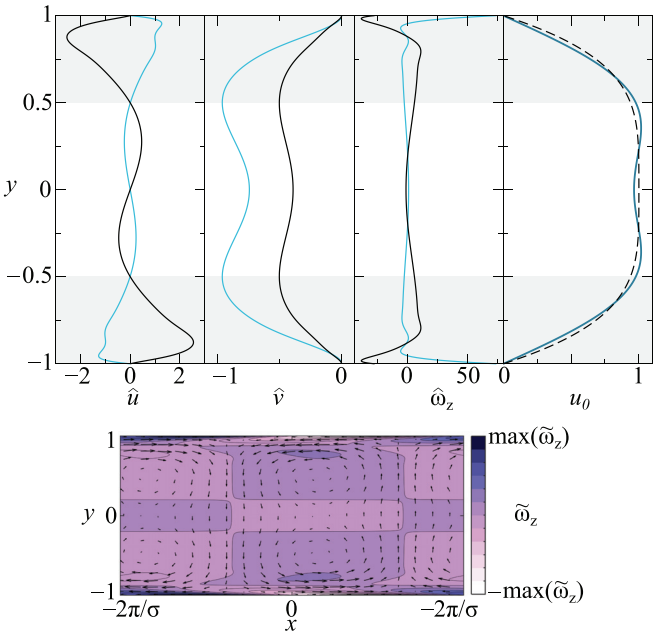

FIG. 9. Top panels: real (black) and imaginary (light blue) parts of the neutral eigenmode in terms of $\hat{u}$ (left), $\hat{v}$ (center-left) and $\hat{\omega}_z$ (center-right), and basic state u_0 (light blue, right) for the generalized Kolmogorov flow for $\alpha = 4$ and $K = 2$. The dashed line in the top-right panel shows the power-law profile for $\alpha = 4$ and the gray stripes highlight the region where the eigenmode admits the highest velocity and velocity gradients. Bottom panel: the most dangerous perturbation depicted in terms of vorticity and velocity field (arrows). Critical conditions for the generalized Kolmogorov flow for $K = 2$ and $\alpha = 4$ are considered.

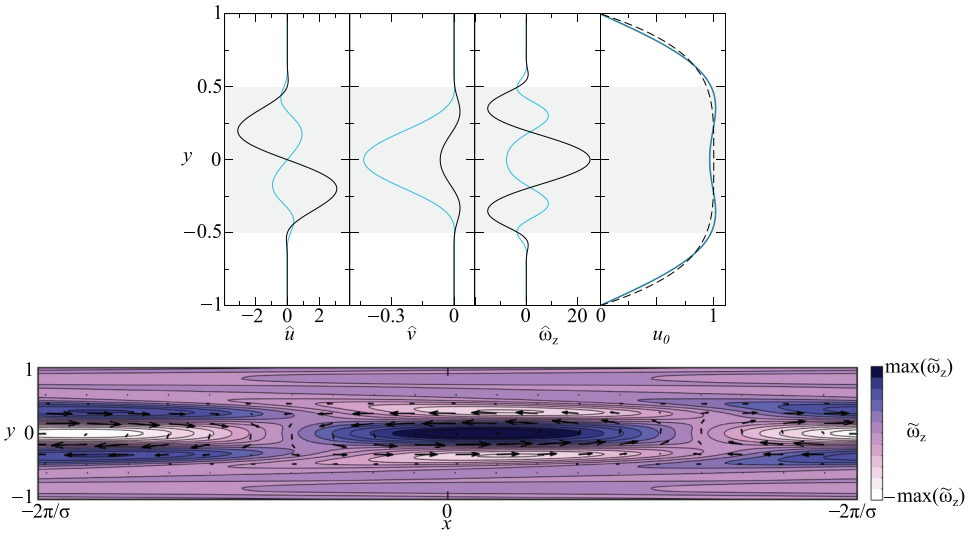

FIG. 10. Top panels: real (black) and imaginary (light blue) parts of the neutral eigenmode in terms of $\hat{u}$ (left), $\hat{v}$ (center-left) and $\hat{\omega}_z$ (center-right), and basic state u_0 (light blue, right) for the generalized Kolmogorov flow for $\alpha = 4$ and $K = 2$. The dashed line in the top-right panel shows the power-law profile for $\alpha = 4$ and the gray stripe highlights the region where the eigenmode admits the highest velocity and velocity gradients. Bottom panel: the most dangerous perturbation depicted in terms of vorticity and velocity field (arrows). Neutral conditions $(\mathrm{Re}, \sigma) = (14\,632,\ 0.50)$ for $K = 2$ and $\alpha = 4$ are considered.

and $(\mathrm{Re}, \sigma) = (366\,400,\ 1.00)$ [Fig. 7(a)] and $(\mathrm{Re}, \sigma) = (\mathrm{Re}_c, \sigma_c) = (219\,483,\ 1.56)$ [Fig. 7(b)]. The same line and color plot style of Fig. 6 is here employed. The top part of the neutral stability curve ($\sigma > 1.16$) is therefore due to the symmetric (even) eigenmode of $\hat{\psi} = -\hat{v}/i\sigma$ [see Fig. 7(b)], whereas the bottom part of the neutral stability curve ($\sigma < 1.16$) is related to the antisymmetric (odd) eigenmode of $\hat{\psi}$ [see Fig. 7(a)].

C. Stability of generalized Kolmogorov flow for even-degree power-law flows

The stability boundaries of the generalized Kolmogorov flow (4) for $\alpha = 4$ and $K = 1, 2, 3, \ldots, 100$ are depicted in Fig. 8(a). The neutral stability boundaries for the $(\alpha = 4)-$ power flow are denoted by the thick solid black line, which confines the unstable region (area filled in light blue). The stability boundaries of the generalized Kolmogorov flow for $K = 1$ (a dark-blue dashed–dotted line) have been discussed in Sec. IV A for $\alpha = 2$. The neutral stability curves for $K = 1$ and $\alpha = 2, 4$ only differ by a scaling factor resulting from (4). For $\alpha = 4$ the first truncation index of (4), $K = 1$, underestimates the critical Reynolds number Re_c of about two orders of magnitude and overestimates the critical wavelength σ_c of about 20% with respect to the power-law profile for $\alpha = 4$ (see Table III). The poor approximation provided by the first truncation index is demonstrated also by comparing the critical eigenspectra of the power-law flow for $\alpha = 4$ [black bullets in Fig. 8(b)] and of (4) for $\alpha = 4$ and $K = 1$ [dark-blue triangles in Fig. 8(b)]. The two eigenspectra are qualitatively different, as the spectrum for $\alpha = 4$ is H-shaped while the spectrum of the generalized Kolmogorov flow for $\alpha = 4$ and $K = 1$ is Y-shaped.

When truncating (4) to the second mode, i.e., $K = 2$, the prediction of the critical Reynolds number is improved of a factor 4 in comparison to the power-law profile for $\alpha = 4$, whereas the critical wavelength worsens, deviating of about 30% from the corresponding σ_c of $u_0 = 1 - y^4$. No remarkable qualitative difference in the critical eigenspectrum is observed between $K = 1$ and $K = 2$. In fact, for $K = 2$ the eigenspectrum [dark-blue squares in Fig. 8(b)] is still Y-shaped as for $K = 1$. The major qualitative difference between the neutral stability boundaries for $K = 1$ and $K = 2$, see dark-blue dashed–dotted and dashed lines in Fig. 8(b), respectively, is due to the presence of a new most dangerous perturbation introduced for $\sigma < 1$ and $\sigma > 1.6$ by the second truncation index of (4). The presence of such a second unstable mode is due to the two symmetric inflection points introduced by the second Fourier mode in the channel bulk. This is demonstrated in Figs. 9 and 10. Figure 9 depicts the critical mode which maximizes the perturbation amplitude near the wall, while Fig. 10 shows the most dangerous perturbation for the neutral stability condition $(\mathrm{Re}, \sigma) = (14632,\ 0.5)$. In this latter case, the perturbation amplitude is maximized in the bulk near the inflection points of the basic state [see Fig. 2(a)].

Upon an increase in the truncation index for $K > 2$, the critical Reynolds number increases monotonically and the critical wavelength decreases monotonically approaching $(\mathrm{Re}_c, \sigma_c)$ for the $(\alpha = 4)$-power-law profile and the truncation indices investigated (see Table III). The two most dangerous modes discussed for $K = 2$ persist for higher K and their footprint on the neutral stability boundaries recedes toward higher neutral Reynolds numbers. For $K = 3$, 4, 5, and 6 a new unstable region emerges at short wavelengths, which region is due to an odd most dangerous eigenmode. The corresponding most dangerous perturbation maximizes the velocity and velocity gradient amplitude near the channel walls and qualitatively resembles the most dangerous perturbation depicted in Fig. 7(a).

The S-branch of the critical eigenspectrum is preserved for $K \leq 2$ and splits into two branches for $K = 3$ at $\Im\{c\} \approx -1.2$ (not shown). Upon an increase in the truncation index, the imaginary part of c at which the S-branch splits reduces in absolute value and gives rise to a K-shaped eigenspectrum for $K = 4$ and to an H-shaped eigenspectrum for $K \geq 5$ [see Fig. 8(b)]. Regardless of the truncation index K, all the critical eigenspectra become unstable at low oscillatory frequencies, along the A-branch. The oscillatory frequency of the most dangerous perturbation decreases monotonically toward $\Re\{c_c\}$ for the $(\alpha = 4)$-power-law profile.

The neutral stability curves for $\alpha = 6$, 8, and 10 are depicted in Fig. 11, together with the stability boundaries for the corresponding generalized Kolmogorov flow (4) truncated at Fourier mode K. In the

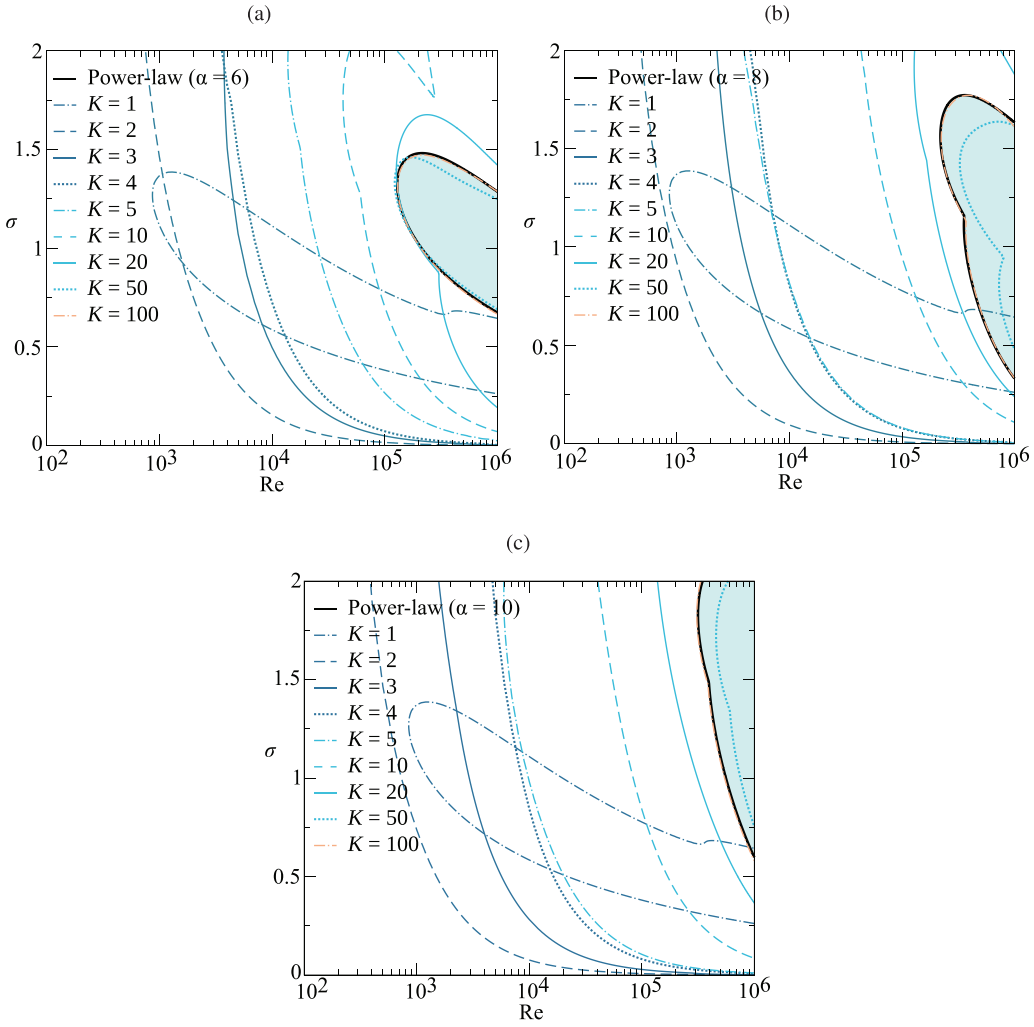

FIG. 11. Neutral stability curves for the power-flow for $\alpha = 6$ (a), $\alpha = 8$ (b), and $\alpha = 10$ (c) (thick black solid line with unstable region filled in light blue) and generalized Kolmogorov flow (4) for $\alpha = 6$ (a), $\alpha = 8$ (b), and $\alpha = 10$ (c) and truncation index: $K = 1$ (dark-blue dashed–dotted line), $K = 2$ (dark-blue dashed line), $K = 3$ (dark-blue solid line), $K = 4$ (dark-blue dotted line), $K = 5$ (light-blue dashed–dotted line), $K = 10$ (light-blue dashed line), $K = 20$ (light-blue solid line), $K = 50$ (light-blue dotted line), and $K = 100$ (peach dashed–dotted line).

light of the stability analysis performed for $\alpha = 4$, the curves for $K = 1$ always admit a Y-shaped eigenspectrum and become unstable with a most dangerous perturbation that admits highest perturbation velocity and velocity gradient near the channel walls. Upon an increase in the truncation index K, the most dangerous mode leading to a bulk instability and correlated with the inflection points of the basic state (see Fig. 10) takes over. This signifies the importance of an inviscid-like instability mechanism related to the Rayleigh's inflection-point criterion. A further increase in K stabilizes the flow moving the unstable region toward higher neutral Reynolds numbers. For a high-enough truncation index K, the wall instability takes over once again such that the most dangerous perturbation admits highest perturbation velocity and velocity gradient near the channel walls. The non-smooth character of the neutral stability curves for high truncation indices K and $\alpha = 8$ and 10 is due to a change of the most dangerous mode, which is symmetric for large wavelengths and antisymmetric for small σ (see Fig. 7).

V. CONCLUSIONS

The stability of shear flows in a channel was investigated considering power-law profiles for $\alpha = 2$, 4, 6, 8, and 10, and generalizing the Kolmogorov flow for even-degree power-law exponents and arbitrary truncation indices. A detailed characterization of the critical eigenspectra, the most dangerous perturbations, and the neutral stability curves was discussed in Sec. IV, comparing the power-law profiles and the generalized Kolmogorov flows for several truncation indices K. Moreover, critical conditions were tabulated whenever the neutral stability curve admitted a turning point.

We further identified the symmetric and antisymmetric most dangerous perturbations determining their influence on the emergence

of two branches of the neutral stability curve for $\alpha \geq 8$. Moreover, also a bulk instability arising for $\alpha \geq 4$ at moderate truncation indices $K > 2$ has been identified and explained in terms of the inflection points of the basic state shear flow profile.[36]

Our investigation was inspired by the several studies that considered the Kolmogorov flow as a paradigmatic model flow for investigating transitional regimes and fully developed turbulence, either in confined or unbounded domains. We therefore expect that our generalization will provide a model flow that can be employed to better understand the effect of linear and non-linear instabilities in transitional regimes of non-Poiseuille-like profiles. The presence of non-linearities becomes relevant when the perturbations considered are no longer infinitesimal. In this case, the convective term in the momentum equation cannot be linearized and the most dangerous perturbation may be other than a plane wave. Such scenarios of transition to turbulence and the identification of coherent structures have been investigated by Chandler and Kerswell[30] in classic Kolmogorov flows and they would be an interesting extension of our study. Other extensions may include the study of non-linear interactions at transitional regimes involving the presence of turbulent puffs and slugs in a laminar surrounding flow. In particular, flat profiles enlarge the linear stability region allowing the study of intermittent flows at higher Reynolds than for a plane Poiseuille flow.[2,39] Such study would connect with the typical flat laminar profiles observed for non-Newtonian pipe and channel flows,[40] allowing to isolate the mean-flow contribution to the laminar-to-turbulent energy transfer from the non-linearity introduced by the non-Newtonian stress tensor.[41–43] Moreover, we think that generalizing the Kolmogorov flow to even-degree power-law profiles of arbitrary order will also help us to shed some light on the relaminarization of turbulent flat flow mean profiles, especially considering the increase in linear stability for $\alpha \uparrow$. In fact, under the assumption that Boussinesq's turbulent viscosity hypothesis holds, the linear stability theory finds application to turbulent flows formally assuming the same equations considered in our study, with the difference that the basic laminar state is replaced by the time-mean flow. In the case of turbulent flows, the quadratic flow fluctuations term are assumed negligible and the Reynolds number is an effective Reynolds number (i.e., it includes the molecular viscosity and the eddy viscosity) and it is a function of space. Finally, the index of truncation K of our generalized formulation (4) can be employed as a control parameter to select the target linear instability of interest for eventual further studies.

DATA AVAILABILITY

The data that support the findings of this study are available from the corresponding author upon reasonable request.

REFERENCES

[1] P. G. Drazin and W. H. Reid, *Hydrodynamic Stability* (Cambridge university Press, 2004).
[2] D. Barkley, "Simplifying the complexity of pipe flow," Phys. Rev. E **84**, 016309 (2011).
[3] Z. S. She, "Large-scale dynamics and transition to turbulence in the two-dimensional Kolmogorov flow,"in CTTR (1988), pp. 374–396.
[4] V. I. Arnol'd and L. D. Meshalkin, "An kolmogorov's seminar on selected problems of analysis (1958/1959)," Usp. Mat. Nauk **15**, 247–250 (1960).
[5] N. F. Bondarenko, M. Z. Gak, and F. V. Dolzhanskii, "Laboratory and theoretical models of plane periodic flow," Izv. Akad. Nauk SSSR, Fiz. Atmos. Okeana **15**, 1017–1026 (1979).
[6] A. M. Obukhov, "Kolmogorov flow and laboratory simulation of it," Russ. Math. Surv. **38**, 113–126 (1983).
[7] J. Sommeria, "Experimental study of the two-dimensional inverse energy cascade in a square box," J. Fluid Mech. **170**, 139–168 (1986).
[8] E. Kazantsev, "Unstable periodic orbits and attractor of the barotropic ocean model," Nonlinear Processes Geophys. **5**, 193–208 (1998).
[9] E. Kazantsev, "Sensitivity of the attractor of the barotropic ocean model to external influences: Approach by unstable periodic orbits," Nonlinear Processes Geophys. **8**, 281–300 (2001).
[10] Y.-K. Tsang and W. R. Young, "Energy-enstrophy stability of β-plane Kolmogorov flow with drag," Phys. Fluids **20**, 084102 (2008).
[11] J. M. Burgess, C. Bizon, W. D. McCormick, J. B. Swift, and H. L. Swinney, "Instability of the Kolmogorov flow in a soap film," Phys. Rev. E **60**, 715 (1999).
[12] L. D. Meshalkin and I. G. Sinai, "Investigation of the stability of a stationary solution of a system of equations for the plane movement of an incompressible viscous liquid," J. Appl. Math. Mech. **25**, 1700–1705 (1961).
[13] V. I. Iudovich, "Example of the generation of a secondary stationary or periodic flow when there is loss of stability of the laminar flow of a viscous incompressible fluid," J. Appl. Math. Mech. **29**, 527–544 (1965).
[14] C. Marchioro, "An example of absence of turbulence for any Reynolds number," Commun. Math. Phys. **105**, 99–106 (1986).
[15] H. Okamoto and M. Shōji, "Bifurcation diagrams in Kolmogorov's problem of viscous incompressible fluid on 2D flat tori," Jpn. J. Ind. Appl. Math. **10**, 191 (1993).
[16] H. Okamoto, "A study of bifurcation of Kolmogorov flows with an emphasis on the singular limit," in Proceedings of the International Congress of Mathematicians (1998), Vol. 3, pp. 523–532.
[17] M. Matsuda and S. Miyatake, "Bifurcation analysis of Kolmogorov flows," Tohoku Math. J., Second Ser. **54**, 329–365 (2002).
[18] K. Nagatou, "A computer-assisted proof on the stability of the kolmogorov flows of incompressible viscous fluid," J. Comput. Appl. Math. **169**, 33–44 (2004).
[19] K. Gotoh and M. Yamada, "The instability of rhombic cell flows," Fluid Dyn. Res. **1**, 165 (1987).
[20] S.-C. Kim and H. Okamoto, "Bifurcations and inviscid limit of rhombic Navier–Stokes flows in tori," IMA J. Appl. Math. **68**, 119–134 (2003).
[21] A. Thess, "Instabilities in two-dimensional spatially periodic flows. Part I: Kolmogorov flow," Phys. Fluids A **4**, 1385–1395 (1992).
[22] Z.-M. Chen, "Instability of the Kolmogorov flow in a wall-bounded domain," J. Phys. Commun. **4**, 015001 (2019).
[23] A. L. Frenkel, "Stability of an oscillating Kolmogorov flow," Phys. Fluids A **3**, 1718–1729 (1991).
[24] G. Boffetta, A. Celani, A. Mazzino, A. Puliafito, and M. Vergassola, "The viscoelastic kolmogorov flow: Eddy viscosity and linear stability," J. Fluid Mech. **523**, 161 (2005).
[25] V. Borue and S. A. Orszag, "Numerical study of three-dimensional Kolmogorov flow at high Reynolds numbers," J. Fluid Mech. **306**, 293–323 (1996).
[26] J. V. Shebalin and S. L. Woodruff, "Kolmogorov flow in three dimensions," Phys. Fluids **9**, 164–170 (1997).
[27] I. E. Sarris, H. Jeanmart, D. Carati, and G. Winckelmans, "Box-size dependence and breaking of translational invariance in the velocity statistics computed from three-dimensional turbulent kolmogorov flows," Phys. Fluids **19**, 095101 (2007).
[28] J. S. A. Green, "Two-dimensional turbulence near the viscous limit," J. Fluid Mech. **62**, 273–287 (1974).
[29] N. Platt, L. Sirovich, and N. Fitzmaurice, "An investigation of chaotic Kolmogorov flows," Phys. Fluids A **3**, 681–696 (1991).
[30] G. J. Chandler and R. R. Kerswell, "Invariant recurrent solutions embedded in a turbulent two-dimensional kolmogorov flow," J. Fluid Mech. **722**, 554–595 (2013).
[31] A. Manela and J. Zhang, "The effect of compressibility on the stability of wall-bounded Kolmogorov flow," J. Fluid Mech. **694**, 29–49 (2012).
[32] F. Gargano, G. Ponetti, M. Sammartino, and V. Sciacca, "Route to chaos in the weakly stratified Kolmogorov flow," Phys. Fluids **31**, 024106 (2019).
[33] S. V. Fortova, "Numerical simulation of the three-dimensional Kolmogorov flow in a shear layer," Comput. Math. Math. Phys. **53**, 311–319 (2013).

[34]S. Berti and G. Boffetta, "Elastic waves and transition to elastic turbulence in a two-dimensional viscoelastic Kolmogorov flow," Phys. Rev. E **82**, 036314 (2010).
[35]K. Roeller, J. Vollmer, and S. Herminghaus, "Unstable Kolmogorov flow in granular matter," Chaos **19**, 041106 (2009).
[36]J. Kühnen, B. Song, D. Scarselli, N. B. Budanur, M. Riedl, A. P. Willis, M. Avila, and B. Hof, "Destabilizing turbulence in pipe flow," Nat. Phys. **14**, 386–390 (2018).
[37]B. J. Bayly, S. A. Orszag, and T. Herbert, "Instability mechanisms in shear-flow transition," Annu. Rev. Fluid Mech. **20**, 359–391 (1988).
[38]T. A. Driscoll, N. Hale, and L. N. Trefethen, "Chebfun guide," (Pafnuty Publications, Oxford, 2014).
[39]S. Gomé, L. S. Tuckerman, and D. Barkley, "Statistical transition to turbulence in plane channel flow," Phys. Rev. Fluids **5**, 083905 (2020).
[40]B. Güzel, I. Frigaard, and D. Martinez, "Predicting laminar–turbulent transition in poiseuille pipe flow for non-newtonian fluids," Chem. Eng. Sci. **64**, 254–264 (2009).
[41]M. Rudman, L. J. Graham, H. M. Blackburn, and L. Pullum, "Non-Newtonian turbulent and transitional pipe flow," in *15th International Conference Hydrotransport* (Citeseer, 2002), pp. 271–286.
[42]S. A. Bahrani and C. Nouar, "Intermittency in the transition to turbulence for a shear-thinning fluid in Hagen-Poiseuille flow," J. Appl. Fluid Mech. **7**, 1–6 (2014).
[43]A. Krishnan Thota Radhakrishnan, C. Poelma, J. Van Lier, and F. Clemens, "Laminar-turbulent transition of a non-Newtonian fluid flow," J. Hydraul. Res. 2020, 1–15.